The Astrophysical Journal, 606:483–496, 2004 May 1

MAGNETOHYDRODYNAMIC MODELS OF THE BIPOLAR KNOTTY JET IN HENIZE 2-90

Chin-Fei Lee and Raghvendra Sahai
Jet Propulsion Laboratory, MS 183-900, 4800 Oak Grove Drive, Pasadena, CA 91109; chin-fei.lee@jpl.nasa.gov, raghvendra.sahai@jpl.nasa.gov
Received 2003 September 9; accepted 2003 November 19

ABSTRACT

A remarkably linear, bipolar, knotty jet was recently discovered in Hen 2-90, an object classified as a young planetary nebula. Using two-dimensional, magnetohydrodynamic simulations, we investigate periodic variations in jet density and velocity as the mechanism for producing the jet and its knotty structures. From a detailed comparison between the Hα emission derived from our models and the observations, we find that a nonmagnetized jet with density or velocity variations does not reproduce in detail the observed structure of the Hen 2-90 jet—a magnetized jet with periodic velocity variations is required. This jet has a radius of 125 AU, an average velocity of 300 km s^{-1} with periodic variations (period = 43 yr) in the jet velocity of amplitude $\pm$15 km s^{-1}, and a toroidal magnetic field with a characteristic strength of 0.6 mG. The average mass-loss rate in the jet has decreased by about a factor of 3 in 600 yr (i.e., from $4.7 \times 10^{-7}\ M_\odot$ yr^{-1} at 20″ to $1.7 \times 10^{-7}\ M_\odot$ yr^{-1} at 1″ from the center along the jet axis). The progenitor asymptotic giant branch wind is assumed to have a mass-loss rate of $1.5 \times 10^{-6}\ M_\odot$ yr^{-1} (derived from the round, tenuous, Hα halo surrounding the central source) and a typical expansion velocity of 10 km s^{-1}. We find a fairly detailed similarity in the physical properties of the jet in Hen 2-90 with that in the young stellar object HH 34. This similarity suggests that the jets in both objects may be launched in a similar manner, namely, from an accretion disk, despite the fact that these objects are at very different evolutionary stages.

Subject headings: stars: AGB and post-AGB — stars: winds, outflows

On-line material: color figures

1. INTRODUCTION

In spite of extensive study, stellar evolution from the asymptotic giant branch (AGB) toward the planetary nebula (PN) stage is poorly understood. The drastic changes observed in circumstellar structure and kinematics (from spherical, slowly expanding AGB envelopes to bipolar PNs with high polar velocities) are particularly puzzling. Recently, based on results of an unbiased survey of young PN morphologies using the *Hubble Space Telescope* (*HST*), Sahai & Trauger (1998) have hypothesized that high-speed jetlike outflows or jets are the primary agent for producing these changes.

However, such jets were not seen directly until recent *HST* imaging of Hen 2-90 in Hα revealed a bipolar jet and a central bipolar nebula bisected by a flaring disklike structure within a round halo (see Sahai & Nyman 2000, hereafter SN00). The jet consists of at least six pairs of evenly spaced knots emanating from the central bipolar nebula. It appears to have not interacted strongly with its surroundings, allowing us to study a post-AGB jet with much less uncertainty than for most PNs (where the jets are visible only via their interaction with the AGB wind). Thus, Hen 2-90 is an important object that can help us to lay the groundwork for constructing jet models of PN shaping.

Knotty jets are seen as Herbig-Haro (HH) objects around young stellar objects (YSOs), tracing internal shocks (or working surfaces) produced by temporal variations in jet velocity (see, e.g., Raga et al. 2002; Reipurth et al. 2002). In these HH objects, shock-excited line emission is usually enhanced. In Hen 2-90, however, no [O III], [O I], or [S II] emission from the knotty structures is detected, and the observed optical lines are narrow (see Guerrero et al. 2001, hereafter G01), both indicating that internal shocks, if present, must be weak and are not responsible for the emission of the knotty structures. In Hen 2-90, a bright hot source is detected at the center of the nebula (SN00; Kaler & Jacoby 1991; Preite-Martínez et al. 1991). Since this hot source is able to fully photoionize the knotty structures seen in the *HST* images (SN00), the emission from the knotty structures is most likely due to photoionized gas. These knotty structures may be produced by temporal variations in jet density or velocity. Currently, the mechanisms that produce variations in jet density/velocity are still not well understood. One possibility is that the jet is driven by an accretion disk in a binary system and that the variations result from a modulation of the accretion process on the orbital timescale.

In this paper, we investigate whether the knotty jet in Hen 2-90 can be produced by simple variations in jet density or velocity using two-dimensional magnetohydrodynamic simulations. In § 2, we describe the properties of the jet and AGB wind in Hen 2-90. In § 3, we describe the numerical method used in our simulations. In § 4, we describe our models, present our simulations, and compare them to the observations of Hen 2-90. In § 5, we discuss our results and previous models proposed for Hen 2-90. In § 6, we summarize and conclude our work.

2. HEN 2-90 OBSERVATIONS

Hen 2-90 is probably located 1–2.5 kpc from Earth (Sahai et al. 2002, hereafter S02); here we assume it to be at 2 kpc. At the center of the bipolar nebula, there is a bright hot source with an effective temperature of 5×10^4 K (Kaler & Jacoby 1991; Preite-Martínez et al. 1991) and a luminosity of $3380(D/2\ \mathrm{kpc})^2\ L_\odot$ (from SN00, but scaled for our slightly different distance).

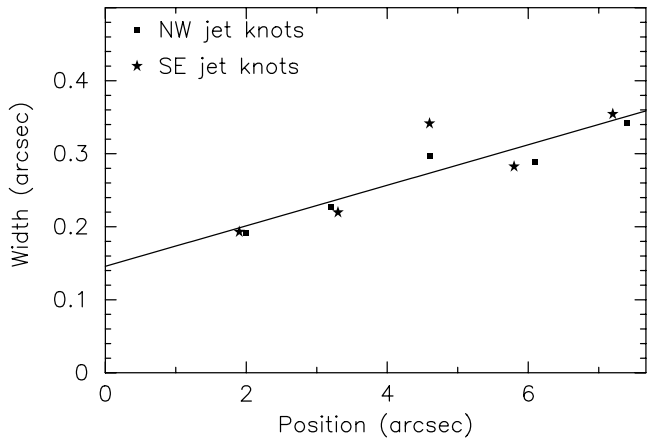

FIG. 1.—Width (FWHM) of the knots in the Hen 2-90 jet measured from the *HST* Hα image in SN00, using Gaussian fitting. The solid line is the best fit to the width with eq. (1).

2.1. *Jet Properties*

The average knot proper motion and radial velocity are found to be $\sim$30 mas yr^{-1} and 26 km s^{-1}, respectively (S02). Thus, the jet velocity is $v_j = 150D$ km s^{-1}, and the inclination of the jet axis to the plane of the sky is $i = \tan^{-1}(0.173/D)$. At $D = 2$ kpc, $v_j = 300$ km s^{-1}, and $i = 5°$.

The (transverse) width (i.e., FWHM with instrumental resolution removed) of the knotty structures perpendicular to the jet axis measured from the *HST* Hα image in SN00 is shown in Figure 1. The width increases roughly linearly with the distance from the source and can be fitted with

$$w = w_0 + \beta d, \tag{1}$$

where w is the width, w_0 is the width at the source, d is the distance from the source, and β is the expansion rate of the width. The best fit is obtained with $w_0 = 0\farcs146$ and $\beta = 0.028$, implying that the jet radius at the source is $R_j \leq 0\farcs073$ or 146 AU, and the apparent transverse expansion velocity of the knot is $v_e = (\beta/2)v_j$ or 4.2 km s^{-1}. The average interknot distance is $\sim$1$\farcs$3, so that the interknot duration is $\sim$43 yr.

In the ground-based observations, the jet is seen at least up to 40″ from the source (S02). The observed line width (FWHM, with instrumental resolution removed) is about 10 km s^{-1} for the [N II] λ6584 line and 20–27 km s^{-1} for Hα (G01).

2.2. *AGB Wind Properties*

The round halo around the central nebula is believed to trace the slowly expanding wind of the progenitor AGB star. This wind is fully photoionized by the hot central source and is assumed to have a temperature of $\sim 10^4$ K. Presumably the AGB wind is radially expanding with the hydrogen number density given by (in spherical coordinates)

$$n_a = n_{a0}\left(\frac{r_0}{r}\right)^2, \tag{2}$$

where $r_0 = 3 \times 10^{16}$ cm (or 1″ at a distance of 2 kpc); n_{a0} can be derived from the *HST* Hα observations. The Hα emission from the AGB wind is likely to be optically thin with the intensity given by

$$I_A(\mathrm{H}\alpha) = \frac{h\nu n_{a0}^2 r_0^4 \alpha}{8d^3} \quad (\mathrm{ergs\ cm^{-2}\ s^{-1}\ sr^{-1}}), \tag{3}$$

where $h\nu$ is the energy of 1 Hα photon, α is the case B recombination coefficient for hydrogen, and d is the projected distance from the central source and assumed to be smaller than the Strömgren radius of the photoionized AGB wind. With $\alpha = 8.6 \times 10^{-14}$ cm^3 s^{-1} at $T = 10^4$ K, we have

$$I_A(\mathrm{H}\alpha) \sim 2.3 \times 10^{-20}\,\frac{n_{a0}^2}{d_s^3} \quad (\mathrm{ergs\ cm^{-2}\ s^{-1}\ arcsec^{-2}}), \tag{4}$$

where d_s is the projected distance in arcseconds. In the *HST* observations, a significant fraction ($\sim$20%–50%) of the detected halo light is due to the wings of the point-spread function of the northwest lobe of the central bipolar nebula (see SN00). Assuming the intensity of this contribution is comparable to that of the AGB wind, the observed intensity of the Hα emission in the halo is

$$I_{\mathrm{obs}}(\mathrm{H}\alpha) = 2I_A + I_b, \tag{5}$$

where I_b is the background level in the observations. Since the density of the AGB wind is proportional to the square root of the observed intensity, this assumption only changes the density of the AGB wind by 30% and thus does not affect our simulation results. The best fit to the observed Hα emission in the halo is shown in Figure 2. It is obtained with $n_{a0} = 3550$ cm^{-3} and $I_b = 1.3 \times 10^{-15}$ ergs cm^{-2} s^{-1} arcsec^{-2}.

Given the He abundance used in our simulations [$n(\mathrm{He}) = 0.1\,n$, where n is the hydrogen number density], the density of the AGB wind is $\rho_a = 1.4 n_a m_{\mathrm{H}}$, where m_{H} is the mass of atomic hydrogen. The mass-loss rate of the AGB wind is

$$\dot{M}_a = 4\pi r^2 \rho_a v_a = 4\pi v_a (1.4 m_{\mathrm{H}} n_{a0} r_0^2), \tag{6}$$

where v_a is the radial expansion velocity of the AGB wind. Assuming $v_a = 10$ km s^{-1}, we have $\dot{M}_a \sim 1.5 \times 10^{-6}\,M_\odot$ yr^{-1}.

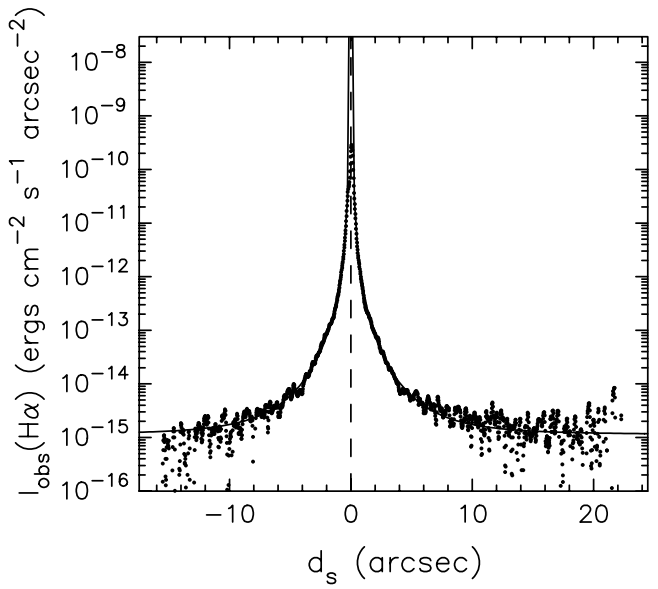

FIG. 2.—Best fit with eq. (5) (*solid line*) to the observed Hα halo emission in the *HST* observations (*points*).

3. NUMERICAL METHOD

The two-dimensional code, ZEUS 2D (Stone & Norman 1992), is used to solve the equations of magnetohydrodynamics,

$$\frac{\partial \rho}{\partial t} + \boldsymbol{\nabla} \cdot (\rho \boldsymbol{v}) = 0,$$
$$\frac{\partial \rho \boldsymbol{v}}{\partial t} + \boldsymbol{\nabla} \cdot (\rho \boldsymbol{v}\boldsymbol{v}) = -\boldsymbol{\nabla} p + \frac{(\boldsymbol{\nabla} \times \boldsymbol{B}) \times \boldsymbol{B}}{4\pi},$$
$$\frac{\partial \boldsymbol{B}}{\partial t} = \boldsymbol{\nabla} \times (\boldsymbol{v} \times \boldsymbol{B}), \quad (7)$$

where ρ, $\boldsymbol{v}$, p, and $\boldsymbol{B}$ are the density, velocity, thermal pressure, and magnetic field, respectively. An isothermal equation of state $p = c_s^2 \rho$ is used for the thermal pressure, where $\rho = 1.4 n m_{\rm H}$, and c_s is the isothermal sound speed. This is reasonable because the central hot source in Hen 2-90 fully photoionizes the material around it; we have therefore assumed the temperature everywhere in our simulation domain to be 10^4 K. The hydrogen is assumed to be fully ionized and the helium is singly ionized, so that the mean molecular mass $\mu = 1.4/2.2$ and $c_s = (kT/\mu m_{\rm H})^{1/2} = 11.4$ km s^{-1} at $T = 10^4$ K. The internal shocks produced in our simulations are very weak and not expected to raise the gas temperature significantly above 10^4 K. This expectation is supported by our test simulations in which cooling was included. Only the leading bow shock formed at the head of the jet has a temperature greater than 10^4 K due to a strong shock interaction. However, this does not affect the conclusions of our paper.

Simulations are performed in cylindrical coordinates with the z-axis aligned with the jet axis. We use a computational domain of dimensions $(z,\ R) = (6,\ 1.5) \times 10^{17}$ cm and a uniform grid of 1200×300 zones. This gives a resolution of 5×10^{14} cm in z and R. Reflecting boundary conditions are used along the inner z and inner R boundaries, while outflow boundary conditions are used along the outer z and outer R boundaries. For $R \leq 2R_j$ along the inner z boundary, inflow boundary conditions are used to introduce a jet into an AGB wind.

4. MODELING

In this section, we describe the parameters of our models and present the results of our simulations. In our models, a cylindrical jet with radius[1] (half of the FWHM) $R_j = 125$ AU and a velocity $v_j = 300$ km s^{-1} is launched at a distance $z_0 = 833$ AU ($\sim 0\farcs4$ at 2 kpc) from the central source into a spherical AGB wind in which $v_a = 10$ km s^{-1} and $\dot{M}_a = 1.5 \times 10^{-6}\ M_\odot$ yr^{-1}. The jet has periodic variations in density and/or velocity with a period $P = 43$ yr. It can be either nonmagnetized or magnetized. For comparing the Hα emission derived from our models to the observations, the former is assumed to be optically thin, and noise is added to our calculations. Position-velocity (PV) diagrams along the jet axis are presented at the spatial resolution of both the *HST* and ground-based observations. Since the [N II] line provides stronger constraints on the line width than the intrinsically much broader Hα line, we have generated PV diagrams from our models for Hα emission, by convolving the model line profiles with the expected thermal line width of [N II] lines (5.7 km s^{-1}) in 10^4 K gas, for comparison with the [N II] data. This procedure is reasonable since the observed spatial distribution of [N II] emission from the bipolar jet is not significantly different from that of Hα (S02).

4.1. *Nonmagnetized Jets*

4.1.1. *Model 1: Density Variations*

In this model, the jet has periodic Gaussian pulses in density (in cylindrical coordinates):

$$\rho_j(R,\ t) = F(R)[\rho_0 + \rho_1 G(t)], \quad (8)$$

where

$$F(R) = \exp[-\ln 2 (R/R_j)^2], \quad 0 \leq R \leq 2R_j, \quad (9)$$

and $G(t)$ is a periodic Gaussian function with

$$G(\tau + iP) = G(\tau) = \exp\left\{-\ln 2 [(\tau - P/2)/t_w]^2\right\},$$
$$i = 0,\ 1,\ 2, \ldots \text{ and } 0 \leq \tau \leq P. \quad (10)$$

Here ρ_0 is a constant for a constant mass loss along the jet axis, while ρ_1 and t_w are the amplitude and half-width of the Gaussian pulse. The jet velocity is held constant during the variation. The initial length (FWHM along the jet axis) of the Gaussian pulse is $l = 2 v_j t_w$. The mass-loss rate in each side of the jet is

$$\dot{M}_j(t) = \int_0^{2R_j} \rho_j(R,\ t) v_j 2\pi R\, dR = \frac{15\pi R_j^2 v_j [\rho_0 + \rho_1 G(t)]}{16 \ln 2}, \quad (11)$$

the average mass-loss rate (averaged over one period) is

$$\langle \dot{M}_j \rangle \simeq \frac{15\pi R_j^2 v_j [\rho_0 + (2t_w/P)\rho_1]}{16 \ln 2}, \quad (12)$$

and each Gaussian pulse has a mass of

$$m_p = \int_0^{2R_j} F(R) 2\pi R\, dR \int_0^P \rho_1 G(\tau) v_j\, d\tau = \frac{15\pi^{3/2} R_j^2 l \rho_1}{32 (\ln 2)^{3/2}}. \quad (13)$$

This model is presented in Figure 3. In this model, $\rho_0 = 1.6 \times 10^{-20}$ g cm^{-3}, $\rho_1 = 1.3 \times 10^{-19}$ g cm^{-3}, and $t_w = 2.15$ yr, giving $l = 271$ AU, $\langle \dot{M}_j \rangle = 2.1 \times 10^{-7}\ M_\odot$ yr^{-1}, and $m_p = 2.7 \times 10^{-6}\ M_\odot$. These parameters are chosen to match the observed Hα intensity and the (longitudinal) length of knot B in the *HST* observations (SN00). As the jet propagates away from the central source into the AGB wind, a bow shock (which has propagated outside our simulation domain and is not shown in the figure) is formed at the head of the jet. The bow shock sweeps up the AGB wind, forming a shell surrounding a low-density cocoon around the jet. The shell expands thermally and eventually merges with the undisturbed AGB wind, becoming indistinguishable from the latter. The variation in the jet density produces a chain of knots moving away from the source along the jet axis. Each knot is associated with a backward and a forward shock. Each knot expands thermally in both the transverse (R) and longitudinal (z) directions, and as it moves away from the source along the jet axis, its head merges with the tail of the knot ahead.

The expansion of knot E (which shows the head-tail structure quite clearly) in the frame moving at the jet velocity is shown in Figure 4. In this frame, the expansion of the knot

[1] The jet has a Gaussian density profile along the R-axis, truncated at $R = 2R_j$.

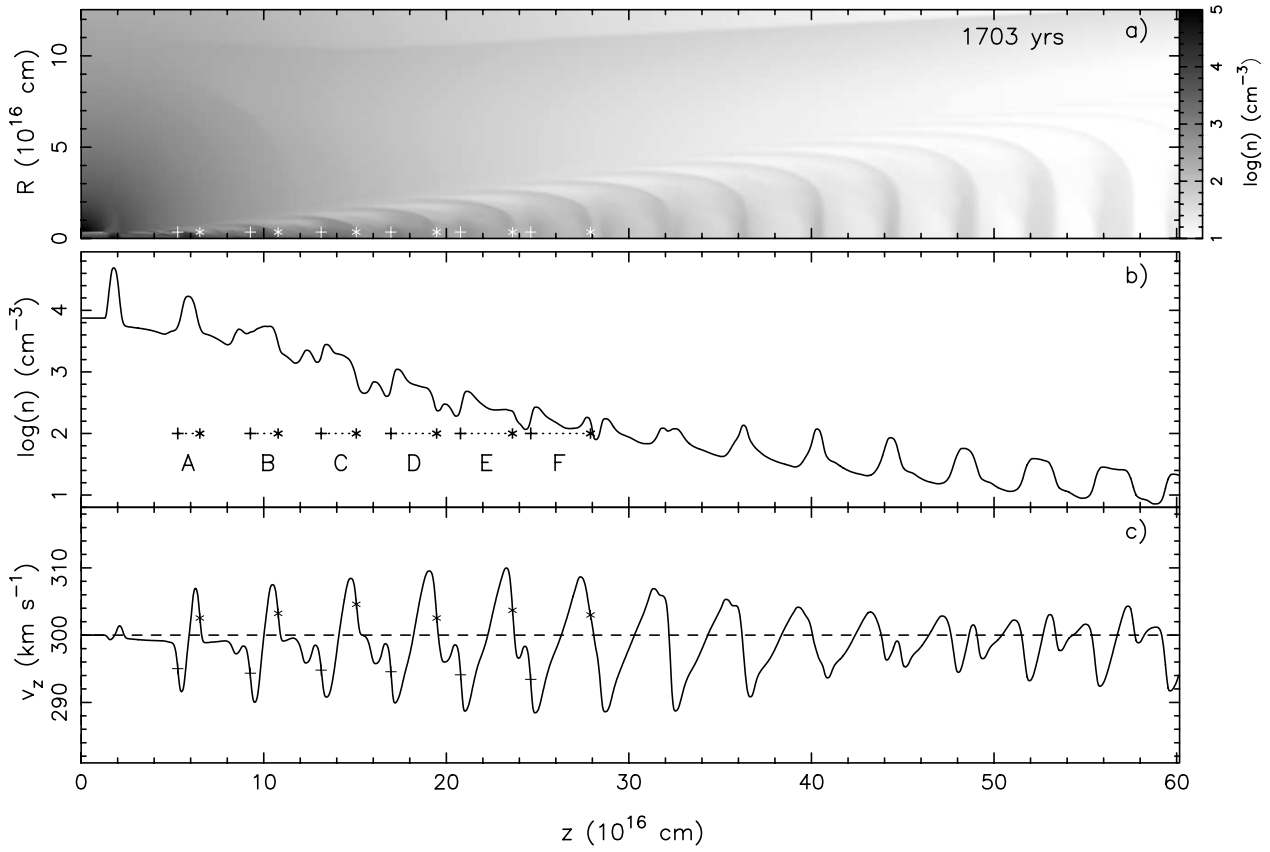

FIG. 3.—Model 1 at the age of 1703 yr. In this model, the jet has a periodic Gaussian variation in density. (*a*) Hydrogen number density (logarithmic stretch). (*b, c*) Number density and longitudinal velocity (v_z) along the jet axis. The crosses and stars indicate the positions of the backward and forward shock fronts in the knots. [*See the electronic edition of the Journal for a color version of this figure.*]

can be regarded as a three-dimensional version of a one-dimensional Sod (1978) shock tube problem. A shock wave propagates away from the knot, shocking and compressing the material outside the knot, while a rarefaction wave propagates toward the center of the knot, causing the knot to expand and the density of the knot to decrease. The shock velocity depends on the density ratio of material inside and outside the knot. In the longitudinal direction, the shock velocity is $\sim$30 km s^{-1}, derived by measuring how fast the separation between the backward and forward shock front

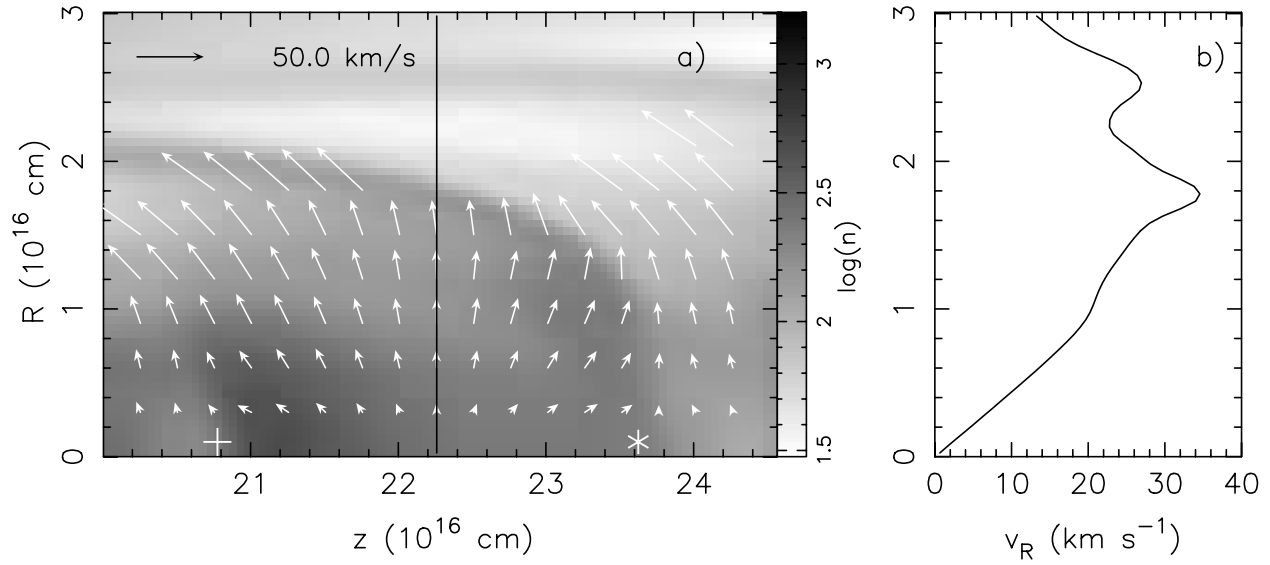

FIG. 4.—Velocity structure of knot E in the frame moving at the jet velocity for model 1. (*a*) Velocity vectors on top of the number density (logarithmic stretch). The cross and star indicate the positions of the backward and forward shocks. The velocity along the solid line is shown in (*b*). [*See the electronic edition of the Journal for a color version of this figure.*]

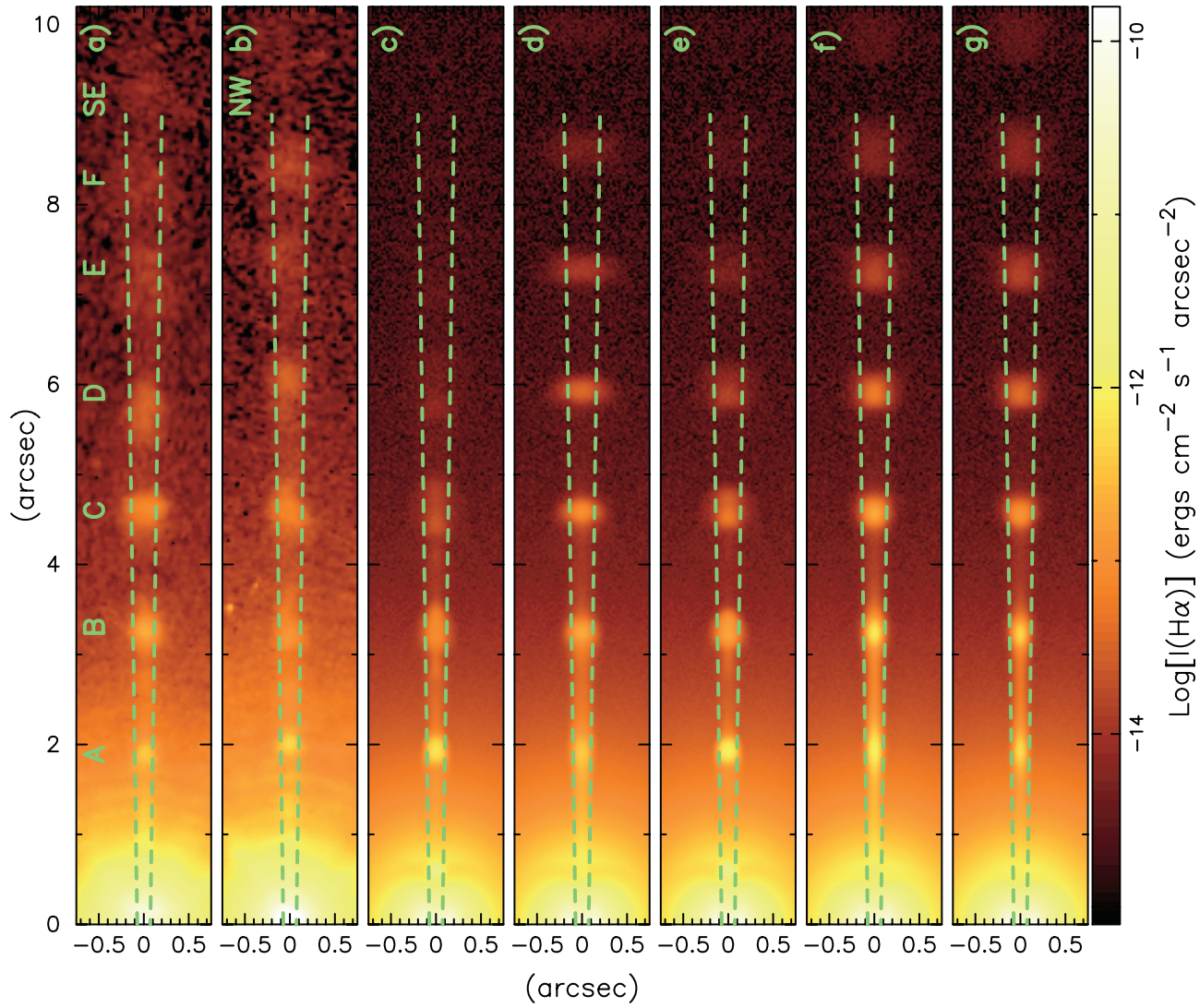

FIG. 5.—*HST* Hα image of Hen 2-90 and models 1–5 (logarithmic stretch). In model 1 (2), the jet has a periodic variation in density (velocity). In model 3, the jet has periodic variations in both density and velocity. In model 4, the jet is the same as that in model 2 but magnetized. In model 5, the jet is the same as that in model 4, but with a average mass-loss rate decreasing with time. (*a, b*) Southeast and northwest jets of Hen 2-90. (*c–g*) Hα emission derived from models 1–5. The green dashed lines delineate a jet opening angle of 2°.

increases from knot A to knot E (see Fig. 3*b*). In the transverse direction, since the curvature decreases with R, the maximum expansion velocity increases with R, and thus with the distance away from the source, it is about twice the sound speed at the position of knot E (see Fig. 4*b*). As the knot propagates away from the source and expands, the density at the center of the knot drops below that at the shocked regions. In addition, because of its thermal pressure, the shocked material at the head of the knot is ejected sideways, forming a bowlike structure at the head and causing the density at the head to drop below that at the tail (see also Fig. 3*b*).

The comparison between the observations of Hen 2-90 and the model in Hα are shown in Figures 5 and 6. The length of the knots increases with the distance in both the observations and model. For a reference, we plot the length of the knots as if the knots expand at twice the sound speed with

$$l(z) = l_0 + 2\frac{c_s}{v_j}(z - z_0), \qquad (14)$$

where $l_0 = 0\farcs21$ and $z_0 = 0\farcs4$. The observed length of the knots can be roughly described by the above simple equation, while the length of the knots in our model is a little larger than the observed length. In addition, the Hα emission for knots C, D, etc., does not peak at the center but at the tail of the knots, inconsistent with the observations. The model Hα intensity decreases with z (i.e., the distance from the center along the jet axis) faster than the observations. This suggests that the average mass-loss rate in the jet was larger in the past. However, such an increase in the average mass-loss rate also increases the density contrast between the material inside and outside the knots, causing both the length and width of the knots to increase faster with z than the observations.

The PV diagrams along the jet axis derived from our model are shown in Figure 7. Each knot is associated with a broad range of velocities centered at 26 km s^{-1}. The emission around zero velocity arises from the cocoon, the AGB wind, and the swept-up shell. In our model PV diagram for the ground-based observations, the FWHM of the [N II] line

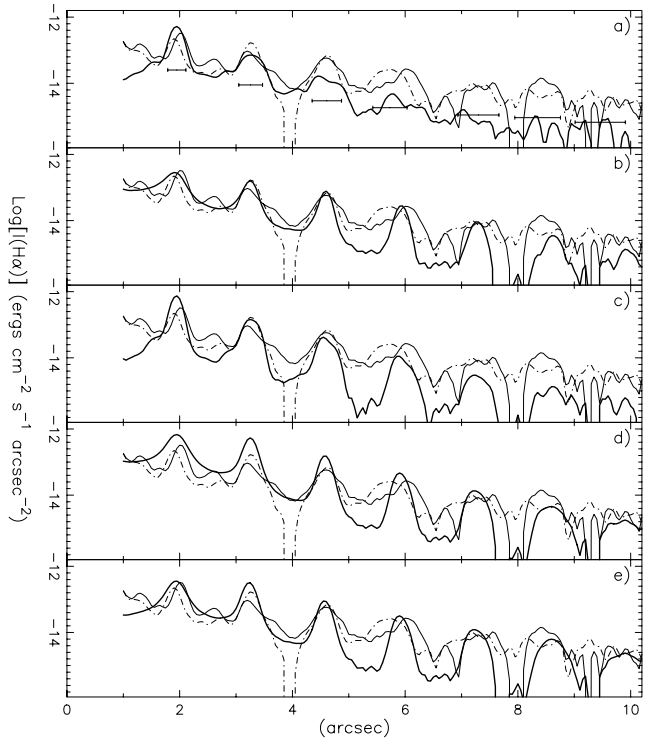

FIG. 6.—Observations and model Hα intensity cuts along the jet axis in Hen 2-90, with the halo emission subtracted. The cuts are 0.″1 wide. The thin solid and dot-dashed curves show the cuts for the southeast and northwest jets in the *HST* image. The thick solid curves in (*a*–*e*) show the cuts for models 1–5. The black lines with the error bars in (*a*) are the reference lengths of the knots calculated with eq. (14). [*See the electronic edition of the Journal for a color version of this figure.*]

profile is about 13 km s^{-1} at knot B (which is in reasonable agreement with the value given in G01) and 22 km s^{-1} at knot C (which is larger than the value in G01; see Figs. 7*b* and 7*c* on the top). Unfortunately, G01 do not specify whether their observed line width applies to a particular knot or to an average over several knots.

4.1.2. *Model 2: Velocity Variations*

In this model, the jet has a sinusoidal variation in velocity:

$$v(t) = v_j - \triangle v \sin(2\pi t/P), \tag{15}$$

where $\triangle v$ is the half-amplitude of the velocity variation. The jet density is constant with time and given by

$$\rho_j(R) = \rho_0 F(R). \tag{16}$$

The average mass-loss rate in each side of the jet is

$$\langle \dot{M}_j \rangle = \int_0^{2R_j} \rho_j(R) v_j 2\pi R dR = \frac{15\pi R_j^2 v_j \rho_0}{16 \ln 2}. \tag{17}$$

This model is presented in Figure 8. In this model, $\triangle v = 15$ km s^{-1} and $\rho_0 = 3.8 \times 10^{-20}$ g cm^{-3} ($n = 1.6 \times 10^4$ cm^{-3}), giving $\langle \dot{M}_j \rangle = 2.7 \times 10^{-7}\ M_\odot\ \mathrm{yr}^{-1}$. These parameters are chosen to produce the observed Hα intensity and the length of knot B. A chain of knots are formed in the jet as the fast-jet material catches up with the slow-jet material. Unlike model 1, however, the backward and forward shock pair does not form immediately (cf. Fig. 8 to Fig. 3). The distance at which the shock pair forms is given by $x_s = [v^2/(dv/dt)]_{\min}$ (see Raga et al. 1990), where the minimum value over the whole period of the jet velocity variation has to be taken. With the velocity given by equation (15), $x_s \sim (v_j^2/\triangle v)(P/2\pi) = 1.3 \times 10^{17}$ cm, consistent with our simulation, in which the shock pair just begins to emerge near knot C. Once the shock pair forms, the separation between the two shock fronts and thus the length of the knot increases with a speed of ∼28 km s^{-1}.

The velocity structure of knot E in the frame moving at the jet velocity is shown in Figure 9. The jet material that goes through the shock fronts into the knot is shocked and ejected sideways, forming a bowlike structure as the knot propagates away from the source. Consisting of the jet material that is thermally expanding, the shocked material is ejected faster than the thermal expansion speed, causing the knot to grow wider than that in model 1 (compare Figs. 4 and 9).

In this model, the decrease of the jet emission with z (and therefore the peak intensity of each jet knot) is in better agreement than model 1 with the observations. However, knots D, E, and F are shorter than those observed in the longitudinal direction. A smaller amplitude velocity variation helps to increase the length of the knots due to a smaller mass flux into the knots; however, it also decreases the knot-to-interknot intensity contrast for knots A and B significantly below what is observed. Similar to those in model 1, each knot is associated with a broad velocity range centered at 26 km s^{-1} (see Fig. 7). In the model PV diagram for the ground-based observations, the FWHM of [N II] line is 14 and 18 km s^{-1} for knots B and C (see middle panels of Figs. 7*b* and 7*c*), similar to that in model 1. We can also measure the FWHM of the line for knots D (30 km s^{-1}) and E (37 km s^{-1}); this was not possible for model 1, where the emission from these knots is too weak and merges with that from the AGB wind and swept-up shell.

4.1.3. *Model 3: Combined Density and Velocity Variations*

A combination of models 1 and 2 may provide a better match to the observations, since in model 1 (2), the knots are longer (shorter) than observed. In this model (model 3), the jet has the same density as in model 1 and the same velocity as in model 2. We find that the resulting structure of the knots is similar to that in model 1. However, because of the periodic variation in the velocity, the interknot jet material now goes through the shock fronts into the knots (compare Figs. 4 and 10), slowing the expansion of the knots in the longitudinal direction. Both the length and width of the knots are now in better agreement with the observations (see Figs. 5 and 6). However, (1) the emission in this model still peaks at the tail of the knots, inconsistent with the observations, and (2) the Hα intensity still decreases with z faster than observed. In the model PV diagram for the ground-based observations, the FWHM of [N II] line is 13, 22, and 32 km s^{-1} for knots B, C, and D, similar to that in models 1 and 2. The emission for knot E is too weak for measuring the FWHM of the line.

In all three models discussed above, the Hα intensity decreases with z faster than observed, probably indicating that the knot material is ejected sideways much too fast into the low-density cocoon. However, because of its low density, the cocoon material does not have enough thermal pressure to confine the transverse expansion of the knots. We are therefore forced to look for an alternative mechanism for knot confinement. An obvious possibility is magnetic tension in a toroidal magnetic field in the jet (see, e.g., Blandford & Payne 1982). It is reasonable to expect that the jet material is magnetized, since most current theoretical models for

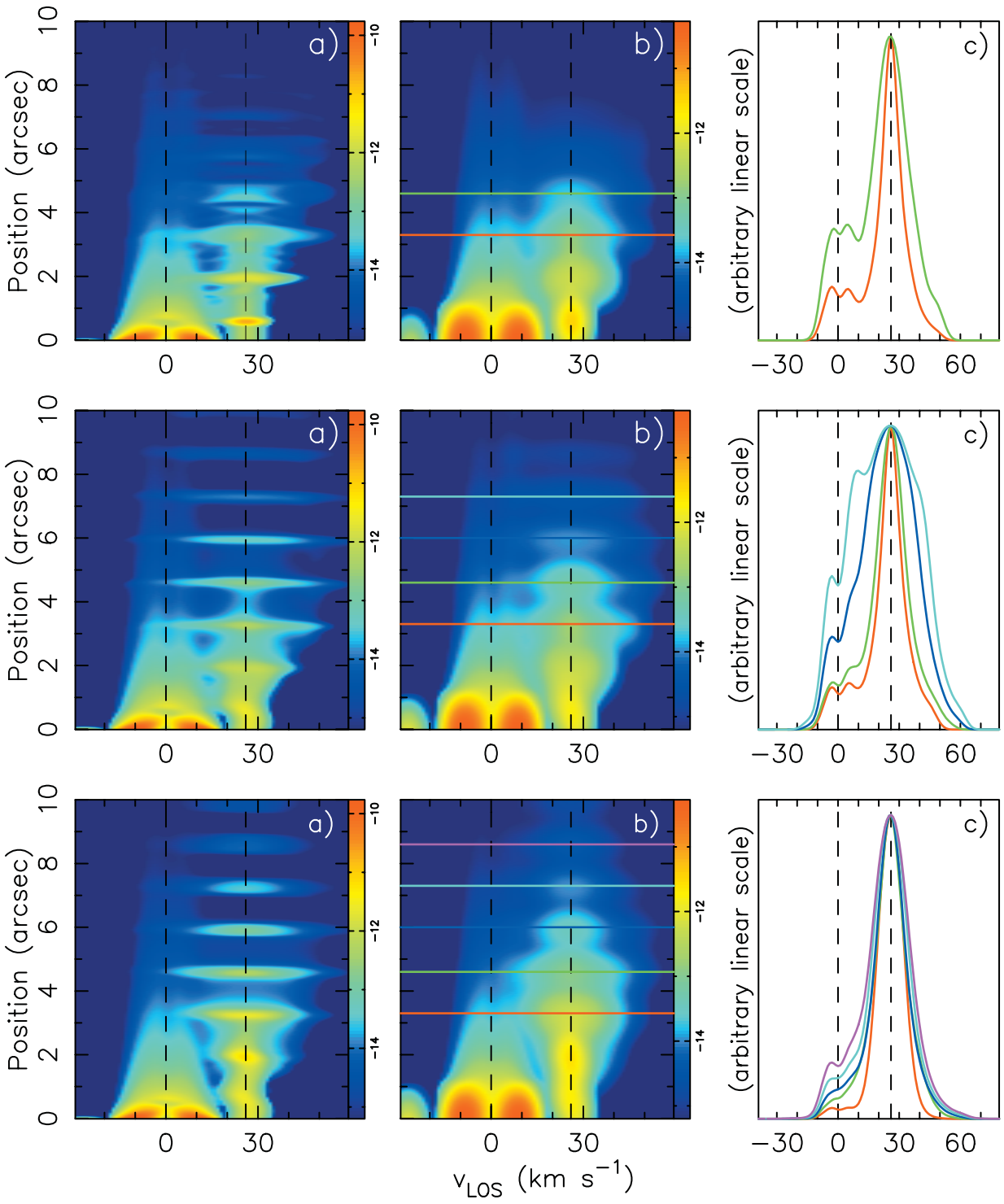

FIG. 7.—PV diagrams of the Hα intensity along the jet axis derived from models 1 (*top*), 2 (*middle*), and 4 (*bottom*). Systemic velocity is set to zero. The models are convolved with the thermal width of [N II] line (or 5.7 km s^{-1}) for comparing with the [N II] observations. (*a*) PV diagram (logarithmic stretch) at a spatial resolution of 0.″08 for comparison with the *HST* observations. (*b*) PV diagram (logarithmic stretch) at a spatial resolution of 0.″9 for comparison with the ground-based observations. (*c*) Velocity cuts across knots B (*red*), C (*green*), D (*blue*), E (*cyan*), and F (*magenta*).

launching astrophysical jets require magnetic fields (see e.g., Shu et al. 2000; Konigl & Pudritz 2000; Blackman, Frank, & Welch 2001).

4.2. *Magnetized Jets*

Here we investigate whether magnetized jets can provide a better match to the observations than achieved thus far in the previous nonmagnetized models. Magnetized jets with periodic variations in density produce emission that peaks at the tails of the knots (similar to that seen in models 1 and 3), inconsistent with the observations. Therefore, we only discuss magnetized jets with periodic variations in velocity.

Since the strength and orientation of the magnetic field in jets is not determined observationally, there is considerable

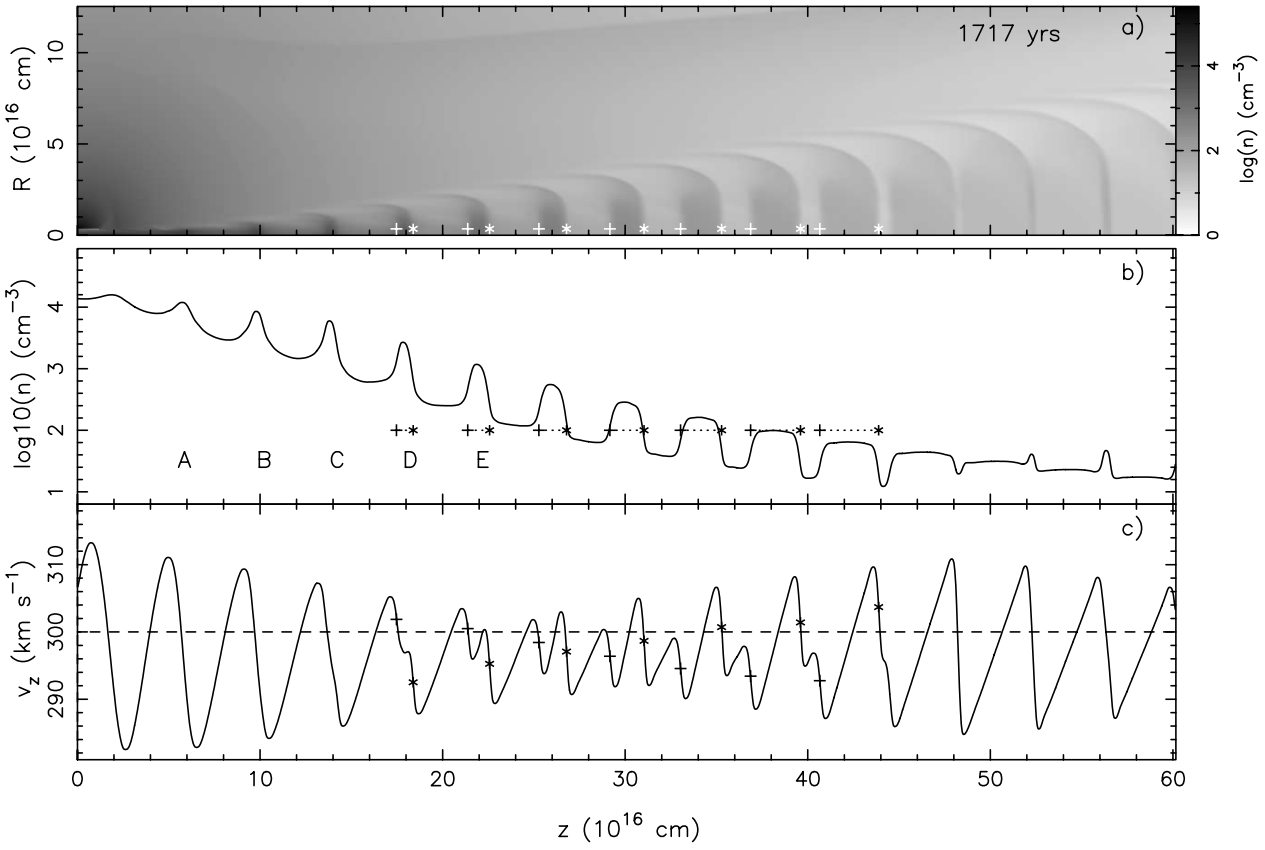

FIG. 8.—Same as Fig. 3, but for model 2. [*See the electronic edition of the Journal for a color version of this figure.*]

freedom in specifying the initial field configuration. In our models, we assume $B_z = B_R = 0$ because theoretical models of magnetically driven jets predict the field should become primarily toroidal asymptotically (Shu et al. 2000; Konigl & Pudritz 2000; Blackman et al.2001). We also assume that the jet is initially in hydromagnetic equilibrium such that the total pressure gradient in the transverse direction is balanced by the magnetic tension due to the toroidal magnetic field, i.e.,

$$\frac{d}{dR}\left[p(R)+\frac{B_\phi^2(R)}{8\pi}\right]=-\frac{B_\phi^2(R)}{4\pi R}. \tag{18}$$

With the density profile given by equation (8), the toroidal magnetic field within the jet is (see Fig. 11)

$$B_\phi(R)=(8\pi p_0)^{1/2}\left\{\frac{1}{aR^2}\left[1-\exp\left(-aR^2\right)\right]-\exp\left(-aR^2\right)\right\}^{1/2}, \tag{19}$$

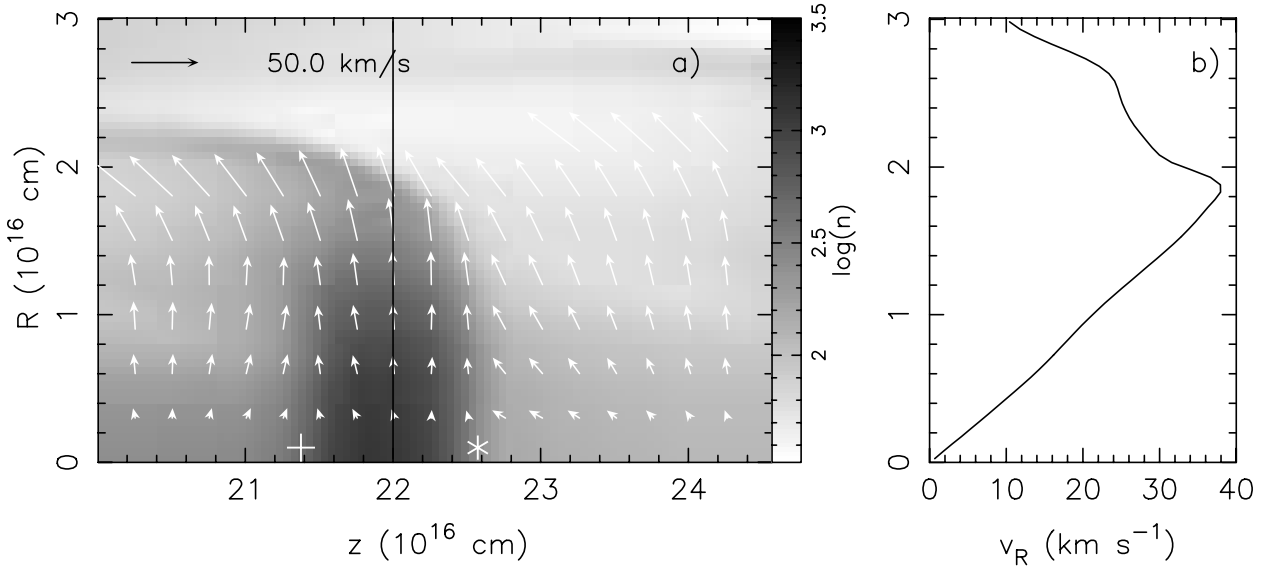

FIG. 9.—Same as Fig. 4, but for model 2. [*See the electronic edition of the Journal for a color version of this figure.*]

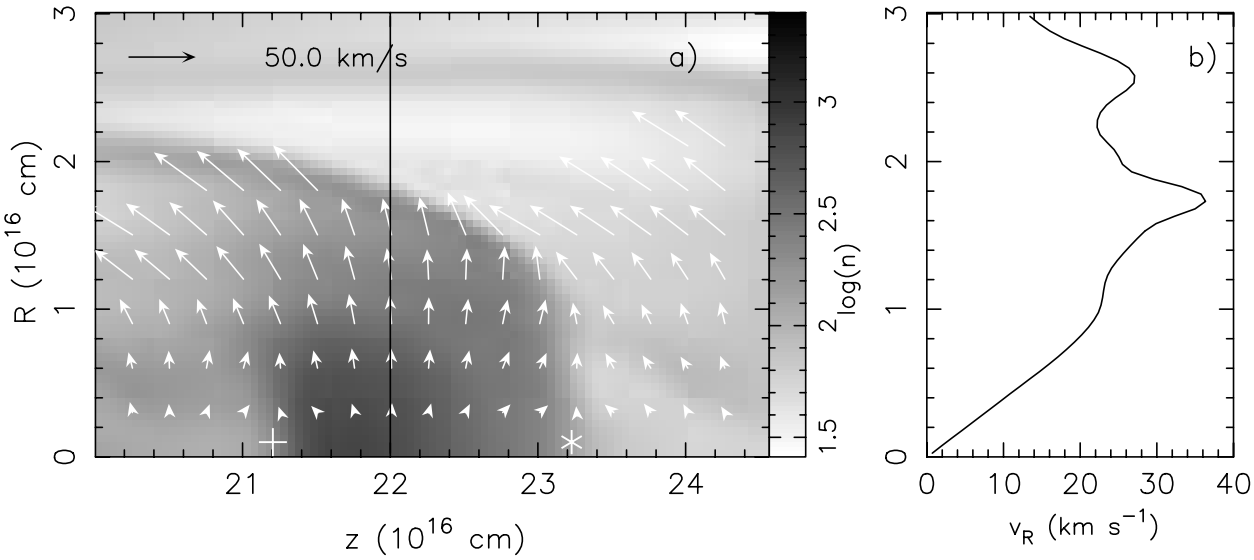

FIG. 10.—Same as Fig. 4, but for model 3. [*See the electronic edition of the Journal for a color version of this figure.*]

where $p_0 = \rho_0 c_s^2$ is the pressure on the jet axis and $a = \ln 2/R_j^2$; $B_\phi = 0$ outside the jet. The magnetic field has a maximum value of $B_{\phi,m} \sim (2.4\pi p_0)^{1/2}$ at $R_m \sim 1.6R_j$. All currents that support the field are confined within the jet (although as the simulation progresses, magnetic field, and therefore current, is convected into the cocoon), and the jet material is self-confined within the jet by its own magnetic field.

Similar profiles of the toroidal magnetic field are used by, e.g., Lind et al. (1989) for their magnetized extragalactic jet models and Stone & Hardee (2000) for their magnetized protostellar jet models. Such a magnetic field configuration could be unstable to current-driven pinch and kink modes. Since our simulations are axisymmetric, we are unable to track kink modes. Begelman (1998) has shown that a jet beam containing a toroidal magnetic field can be unstable to current-driven pinch modes when

$$\frac{d\ln B}{d\ln R} > \frac{\gamma\beta - 2}{\gamma\beta + 2}, \tag{20}$$

where $\beta \equiv 8\pi p/B^2$. This condition is satisfied for our adopted initial field configuration. In a steady jet simulation with this field configuration, the pinch mode instability causes an initial collapse of the jet beam toward the polar axis. Under appropriate physical conditions (low jet Mach number $\sim$10 and low $\eta \sim 1.5$, the ratio between the jet density and ambient density), this collapse then produces a series of strong shocks and reflections in the jet as it propagates, resulting in a series of periodic density enhancements (Frank et al. 1998). In our models, both the Mach number and η are much higher (30 and 10, respectively); hence, the effect of the pinch mode instability is much weaker (Cerqueira & de Gouveia dal Pino 1999). Furthermore, pinch modes are found to be saturated at low amplitude in the nonlinear regime (Stone & Hardee 2000), so it is unlikely that they can produce the density enhancements represented by the observed knots in Hen 2-90. In addition to current-driven instabilities, magnetized jets can also have velocity-driven MHD Kelvin-Helmholtz instabilities (Cerqueira & de Gouveia dal Pino 1999). However, these grow relatively slowly for high Mach number axisymmetric flows (Stone & Hardee 2000), as is the case for the Hen 2-90 jet. Nevertheless, in view of the many MHD simulation studies directed toward explaining knotty protostellar jets (e.g., Cerqueira & de Gouveia dal Pino 1999; Frank et al. 1998, 2000), magnetic field instabilities should be investigated further (e.g., with different magnetic field strength and configurations) as an alternative mechanism for producing the Hen 2-90 knotty jet.

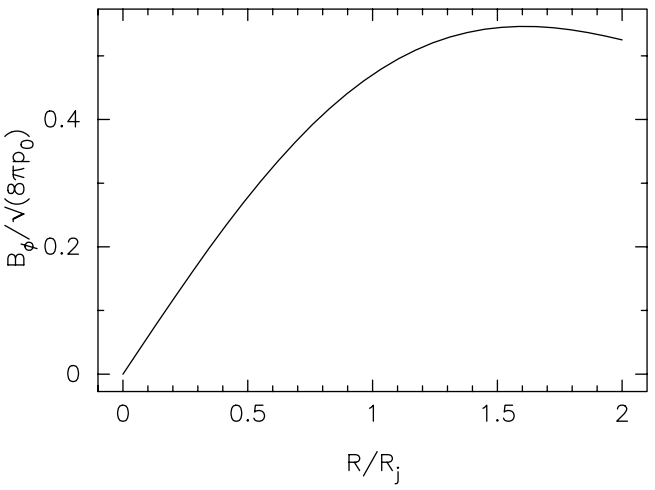

FIG. 11.—Radial profile of the toroidal magnetic field inside the jet

4.2.1. *Model 4: Velocity Variations*

In this model, the jet is launched with the same physical structure as in model 2 but magnetized with $B_{\phi,m} \sim 0.6$ mG. The jet material close to the jet axis is confined by the toroidal magnetic field, showing a density higher than that in model 2 (see Fig. 12). The resulting knots are narrower in the transverse direction and in better agreement with the data than model 2 (see Figs. 5 and 6). Because of the increase of the total pressure (magnetic pressure+thermal pressure) inside the knots, the length of the knots increases with z faster than model 2 and is also in better agreement with the observations. In the model PV diagrams for the ground-based observations, the FWHM of the [N II] line profile for knots A–F is 14–20 km s^{-1} (see Fig. 7), smaller than that in model 2. However, the knot emission in this model still decreases faster with z than

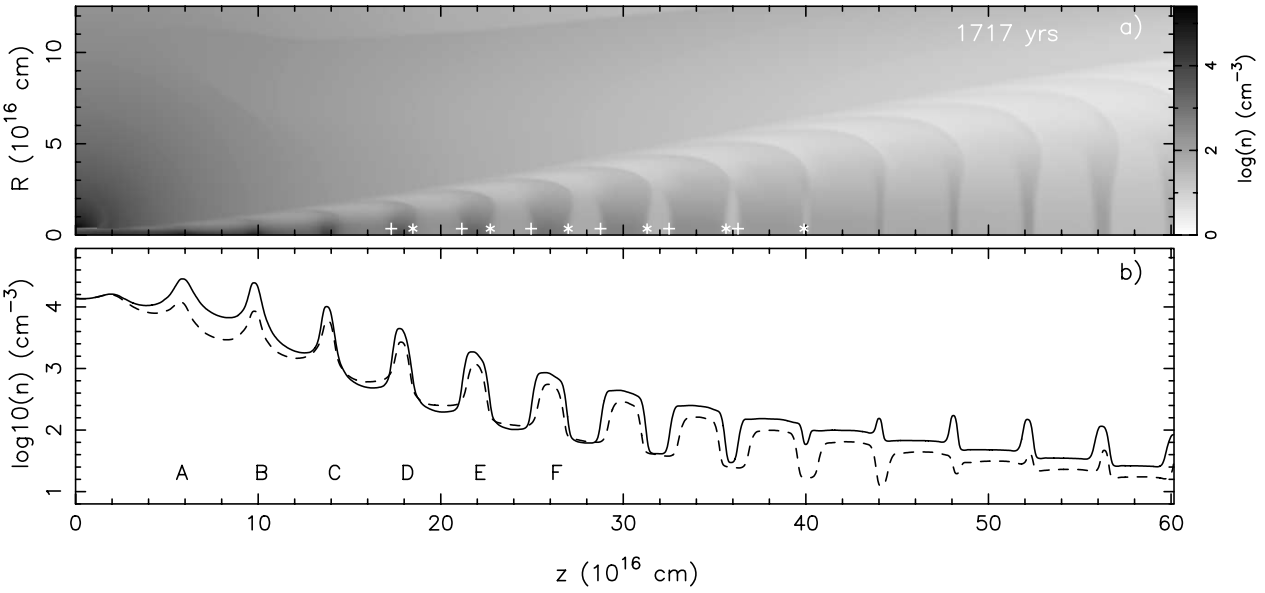

FIG. 12.—Model 4 at the age of 1717 yr. The jet in this model is the same as that in model 2 but magnetized. (*a*) Number density (logarithmic stretch). The crosses and stars indicate the positions of the backward and forward shock fronts in the knots. (*b*) Number density along the jet axis; the solid curve represents model 4 and the dashed curve represents model 2. [*See the electronic edition of the Journal for a color version of this figure.*]

observed. A stronger toroidal magnetic field may further confine the knot material and improve the z dependence of the knot emission; however, it would make the knotty structures narrower and longer than observed.

4.2.2. *Model 5: Long-Term Change in the Jet Mass-Loss Rate*

In this model, in order to produce stronger emission far away from the source, we increase the average mass-loss rate in (and thus the density of) the jet in the past as

$$\rho_j(R,\ t) = \rho_0 F(R)(3.5 - t/t_0), \qquad (21)$$

where the timescale $t_0 = 540$ yr. The Hα emission derived from this model at the age of 1588 yr is shown in Figures 5, 6, and 13. The average mass-loss rate in the jet decreases by about a factor of 3 in 600 yr (i.e., from $4.7 \times 10^{-7}\ M_\odot\ \mathrm{yr}^{-1}$ at $20''$ to $1.7 \times 10^{-7}\ M_\odot\ \mathrm{yr}^{-1}$ at $1''$ from the center along the jet axis). We compare our model Hα emission to the ground-based observations because the latter shows emission from the jet to a much larger distance from the center than the *HST* observations, providing a stronger constraint on the long-term mass-loss history of the jet. This adopted decrease in the average mass-loss rate produces roughly the observed decrease of Hα emission with z in the ground-based and *HST* images. The PV diagrams for this model are similar to that for model 4.

5. DISCUSSION

5.1. *Our Models*

Our modeling has shown that a nonmagnetized jet with density or velocity variations does not reproduce in detail the observed structure of the Hen 2-90 jet. However, a magnetized jet with small periodic variations in velocity can roughly produce the knotty structures seen in Hen 2-90. In order to produce the decrease in jet emission with distance from the center, the average mass-loss rate in the jet has to have steadily decreased with time (i.e., was higher in the past). This decrease in the mass-loss rate may result from a decrease in the accretion rate onto an accretion disk in a binary system (SN00). For example, in the case of YSOs, the observed accretion rate is known to decrease with time as the infall rate from the collapsing envelope decreases (Hartmann et al. 1998; Calvet, Hartmann, & Strom 2000).

The jets, which are thought to be responsible for the shaping of PNs, are seldom seen directly in proto-planetary nebulae (PPNs) and PNs, because they interact strongly with the dense ambient medium resulting from the progenitor AGB

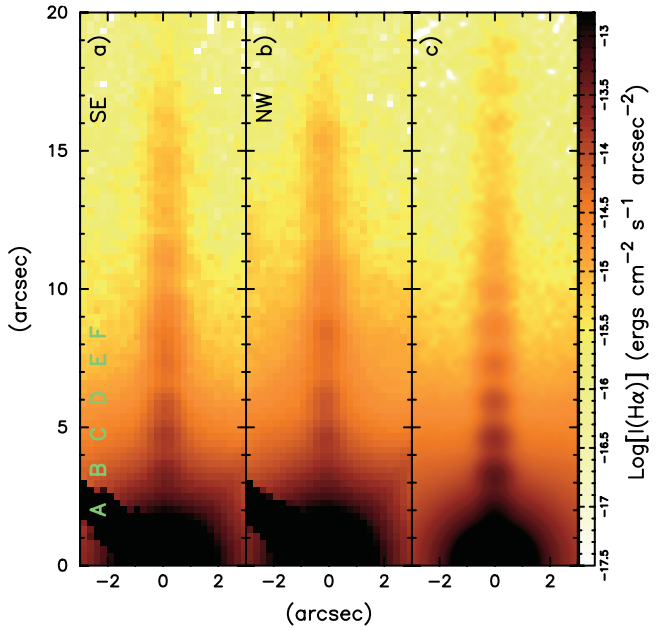

FIG. 13.—Comparison of model 5 with the ground-based Hα image (logarithmic stretch). (*a, b*) Southeast and northwest jets of Hen 2-90. (*c*) Hα emission derived from model 5 at a spatial resolution of $0\farcs9$.

winds in these objects. The interaction produces elongated shells of swept-up ambient material. Hen 2-90 appears different from other young PNs because it shows the jet very clearly, but there is no evidence of the swept-up shell. We think that the main reason for this is because the AGB wind in our models is rather tenuous ($\dot{M}_a \sim 10^{-6}\ M_\odot\ \mathrm{yr}^{-1}$), and thus there is not enough material in the shell. The PN shells produced by the Generalized Interacting Stellar Winds model (e.g., Mellema & Frank 1995), in which the AGB wind is similarly tenuous, are more massive because they are produced by an *intrinsically isotropic* fast wind that can sweep up much more ambient material. An additional possibility is that since the ambient material is hot during the formation of the shell in Hen 2-90 (because it is assumed to be photoionized), the consequent lack of cooling prevents the shell from collapsing into a thin dense structure. In contrast, for typical PNs that are not currently ionization-bounded, the ambient material was probably cold during shell formation, resulting in significant cooling and the formation of a thin dense shell; this possibility needs to be investigated using hydrodynamic simulations.

While it is true that instabilities and/or turbulence in interacting flows can lead to knotty structures, we believe that these are not the cause of the knots in the Hen 2-90 jet, which have (1) rather uniform spacing, (2) well-formed shapes, and (3) the same proper motion for knots spanning a very large dynamical age range. Although we have found reasonably good model fits to the observations, the following issues need further investigation.

5.1.1. *Leading Bow Shock*

A leading bow shock is expected to be present at the tip of the jet, due to its interaction with the tenuous AGB wind. However, we cannot pinpoint the location of this bow shock in the ground-based images because we do not know the actual age of the jet (we only have a lower limit ~1400 yr, S02). If, for example, the jet was 1700 yr old, then the leading bow shock would be seen as a round blob at the spatial resolution of the ground-based observations 48″ from the central source (see Fig. 14). However, such bow shock emission is currently undetected in the ground-based image, which covers a very large field of view (~10′; S02); it is likely that the former lies outside the Strömgren radius along the jet axis.

We now quantitatively show that the above is a reasonable hypothesis, using the photoionizing flux and the density structure of the jet. Defining $S(r)$ as the total number of photons flowing through a shell of radius r per second with a frequency greater than that at the Lyman limit, we have

$$\frac{dS(r)}{dr} = -4\pi r^2 n_e n_p \alpha^{(2)}, \tag{22}$$

where $\alpha^{(2)}$ is the recombination coefficient excluding captures to the $n = 1$ level, n_e (n_p) is the electron (proton) number density along the jet axis. For simplicity, the density in our models can be approximated as

$$n_e \sim n_p \equiv n_{j0}\left(\frac{r}{r_0}\right)^{-(1+q)}, \tag{23}$$

so that

$$\frac{dS(r)}{dr} = -4\pi n_{j0}^2 r_0^{2+2q} \alpha^{(2)} r^{-2q}. \tag{24}$$

Since the starting distance of the jet is unknown and equation (23) may not apply to the jet close to the source, we define a radius r_i, such that $S(r_i)$ can be equated to the total number of ionizing photons emitted per second from the central source, and beyond which equation (23) is applicable. Integrating equation (24) over r from r_i to the Strömgren radius, r_S, and solving for r_i, we have

$$r_i = r_S\left\{\left[1 + \frac{S(r_i)}{4\pi n_{j0}^2 r_0^2 r_S (r_0/r_S)^{2q}\alpha^{(2)}/(2q-1)}\right]^{-1}\right\}^{1/(2q-1)}. \tag{25}$$

Assuming an effective temperature of 5×10^4 K and a luminosity of 3380 $L_\odot$ for the source, $S(r_i) = 2.3 \times 10^{47}\ \mathrm{s}^{-1}$. At 10^4 K, $\alpha^{(2)} = 2.8 \times 10^{-13}\ \mathrm{cm}^3\ \mathrm{s}^{-1}$. In our best-fit model (model 5) for Hen 2-90, $q \sim 0.8$, $r_0 = 3 \times 10^{16}$ cm, and $n_{j0} \sim 2 \times 10^4\ \mathrm{cm}^{-3}$. In order for the Strömgren radius in

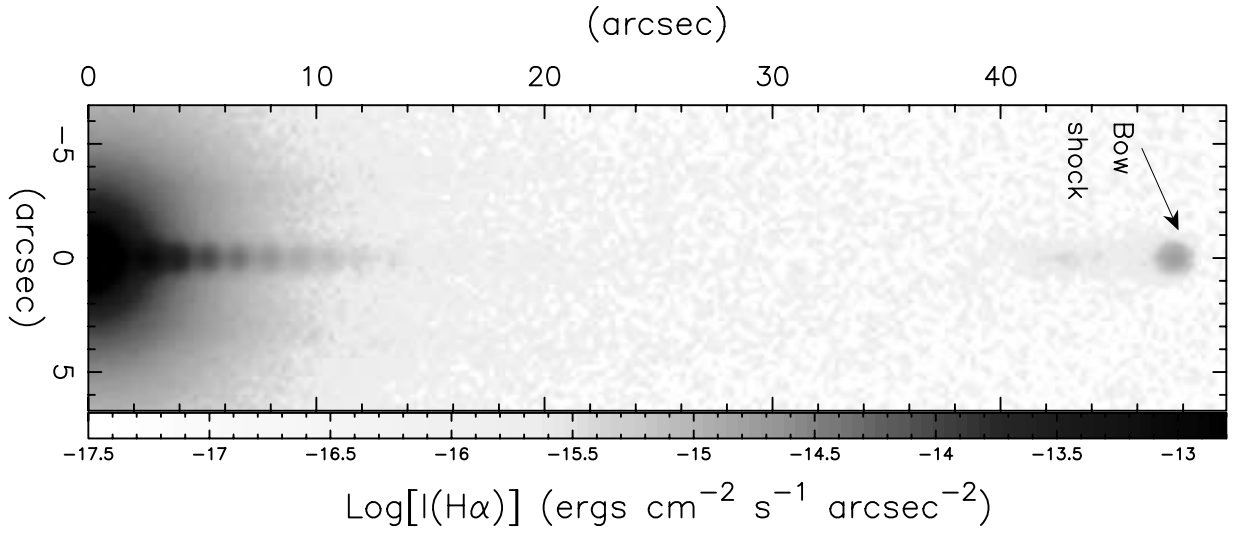

FIG. 14.—Hα image (logarithmic stretch) derived from model 4 at the age of 1700 yr as seen in the ground-based observations at a spatial resolution of 0″.9. The simulation for this model is performed with 2.5 times larger domain but 1.5 times lower resolution than in the other models. [*See the electronic edition of the Journal for a color version of this figure.*]

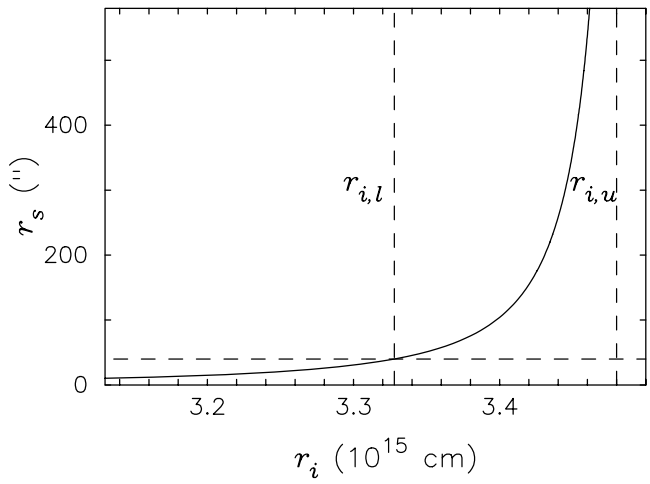

FIG. 15.—Relationship between the Strömgren radius (r_S) and the radius r_i, derived from eq. (25). The horizontal dashed line corresponds to $r_S = 40''$.

Hen 2-90 to be greater than the observed length of the jet ($\approx 40''$; S02), $r_S \gtrsim 40''$ (i.e., 1.2×10^{18} cm). Hence, from equation (25), $r_i \gtrsim 3.3 \times 10^{15}$ cm ($\equiv r_{i,l}$, $\sim$220 AU or $0''.11$); i.e, no significant attenuation of the ionizing flux has occurred out to this radius. This value of r_i is reasonable because, for example, in order to produce a 10% reduction in the photoionizing flux upto r_i, the average electron density at r_i has to be $\sim 7 \times 10^5$ cm^{-3} (from eq. [22], assuming constant electron density for $r \leq r_i$). This value is more than 60 times higher than the value of n_e at the jet injection radius in our best-fit model, which implies a current jet mass-loss rate 60 times larger than that at the epoch corresponding to the jet injection radius. This is very unlikely because we have shown that the jet mass-loss rate is actually decreasing with time.

In order for the leading bow shock to lie outside the Strömgren radius, as hypothesized earlier, r_S must be finite. However, because $r_S \rightarrow \infty$ as $r_i \rightarrow 3.5 \times 10^{15}$ cm ($\equiv r_{i,u}$; see Fig. 15), significant attenuation of the ionizing flux must occur in the inner regions of the jet (near $r_{i,u}$). Although $r_{i,u}$ is uncomfortably close to $r_{i,l}$, this is simply an artifact of extrapolating our derived (rather steep) density law to the inner regions of the jet. For example, a flatter density law would increase the separation between $r_{i,l}$ and $r_{i,u}$. The detailed knowledge of where the attenuation of the ionizing flux occurs depends on a correspondingly precise knowledge of the jet density structure in its inner regions, which is currently unknown.

5.1.2. *Line Widths*

Our models of magnetized jets produce smaller line widths than those of nonmagnetized jets because of the magnetic confinement by the toroidal field. The Hα line widths in these models lie in the range 25–29 km s^{-1}, a little larger than the observed width (20–27 km s^{-1}) in the ground-based observations. In addition, the knotty structures in Hen 2-90 and our models of magnetized jets show a similar opening angle, which implies, given the jet speed, that the transverse expansion rate of the knots in our model is consistent with the knots in the Hen 2-90 jet. However, the [N II] line widths in these models (14–20 km s^{-1}) are still discrepant from the observed width ($\sim$10 km s^{-1}) in the ground-based observations. Since the model line widths depend in detail on the density and velocity distribution within the knots, it is possible that fine-tuning of these distributions (by, e.g., varying the functional form of the toroidal magnetic field) may help in resolving this discrepancy.

5.2. *Previous Models for Hen 2-90*

It was once proposed by García-Segura, López, & Franco (2001) that the knots in Hen 2-90 are self-collimated gaseous structures along the polar axis within a strongly magnetized AGB wind. As argued by S02, this model is invalid for Hen 2-90 because it predicts that the knots should be moving at the expanding velocity of the AGB wind (typically 10–20 km s^{-1}), contrary to that inferred from recent observations ($\sim$150–360 km s^{-1}; S02).

Recently, García-Segura, López, & Franco (2003) have proposed a new model for Hen 2-90, in which the jet knots are produced by magnetic collimation (pinching) within a fast-moving spherical post-AGB wind that blows from the stellar surface into a nonmagnetized AGB wind with an equatorial density enhancement. A periodic variation in magnetic field strength produces a chain of symmetric and equidistant knots along the polar axis, apparently resembling the ones observed in Hen 2-90. In this model, the post-AGB wind is spherical, and the jet is formed along the axis by magnetic collimation. Unfortunately, García-Segura et al. (2003) have not given detailed results from their modeling for comparison with the observations, so it is difficult to evaluate its merit or compare it with our modeling. However, we note that the knotty structures in their model are not resolved in their numerical grid; thus, the opening angle of their model jet is constrained by the numerical resolution. In addition, their model shows a dense shell surrounding the jet (Fig. 2 in their paper), which is not seen in the data.

5.3. *Similarity to YSO Jets*

HH objects around many YSOs also appear as knotty structures similar to the knots seen in the Hen 2-90 jet. In this context, HH 34 (Reipurth et al. 2002) is one of the best such examples. We compare the properties of its jet to that of Hen 2-90 in Table 1. The chain of knots in HH 34 has been modeled by Raga et al. (2002) using hydrodynamic simulations assuming a periodic velocity variation as in our study of Hen 2-90. Although the apparent transverse expansion velocity of the knots in HH 34 (1.5 km s^{-1}) is lower than in Hen 2-90 (4.2 km s^{-1}), this difference may be related to the significantly lower temperature of the knots in HH 34 (which are mostly neutral) compared to the much hotter, photoionized knots in Hen 2-90.

The detailed similarity between the jets in these two objects suggests that the launching mechanism for the jets may be the

TABLE 1
COMPARISON BETWEEN HEN 2-90 AND HH 34

Parameter	Hen 2-90	HH 34
Adopted distance (pc)	2000	460
Jet speed (km s^{-1})	300	215[a]
Jet width at the source (AU)	292	110[a]
Apparent transverse expansion velocity (km s^{-1})	4.2	1.5[a]
Period (yr)	43	27[b]
Velocity variation $\triangle v$ (km s^{-1})	15	10[b]
Average jet mass-loss rate (10^{-7} $M_\odot$ yr^{-1})	1.7–4.7	1.7[c]

[a] From *HST* observations by Reipurth et al. 2002.
[b] From numerical modeling by Raga et al. 2002.
[c] From Hartigan, Morse, & Raymond 1994.

same, despite the fact that they are at very different evolutionary stages. Since the jets in both HH 34 and Hen 2-90 appear to have fairly large diameters (Table 1) close to the region from where they are launched, it is plausible that these jets start out as wide but collimated flows from accretion disks in binary systems (Konigl & Pudritz 2000; Blackman et al. 2001). In addition, for both objects, the variability in jet velocity that produces the knots may be due to perturbation of the accretion disk in an eccentric binary system; in this case, the period of the velocity variation is equal to the orbital period of the binary. The central star in HH 34 has been proposed to be a binary (Reipurth, Bally, & Devine 1997; Reipurth et al. 2002). The slight S-shaped wiggle seen in HH 34 is generally ascribed to the tidal effects of the companion star on the direction of the jet axis. Such an S-shaped wiggle, however, may be too small to be seen in Hen 2-90 (S02).

5.4. *Jet Mass-Loss Rate in Hen 2-90*

In our best-fit model (model 5), each side of the jet has a mass-loss rate decreasing from 4.7 to $1.7 \times 10^{-7}\ M_\odot\ \mathrm{yr}^{-1}$. This mass-loss rate is about 1 order of magnitude higher than that calculated in SN00, which (1) had a factor of 4 error in the jet cross section used in their calculation (R. Sahai 2003, private communication), (2) used the then best estimate of the jet velocity (150 km s^{-1}), which is a factor of 2 lower than the current value, and (3) did not account for the He abundance. It has been proposed that the jet is launched from an accretion disk that is formed by gravitational capture of the progenitor AGB wind onto a companion in a binary system (Morris 1987). Since most MHD launching mechanisms yield $\dot{M}_j \sim 0.1\dot{M}_{\rm acc}$ (Konigl & Pudritz 2000), the expected $\dot{M}_j \sim 0.1\alpha\,\dot{M}_a$, where α is the ratio of the mass-accretion rate ($\dot{M}_{\rm acc}$) to the AGB mass-loss rate ($\dot{M}_a$). Given that the AGB mass-loss rate in Hen 2-90 is only $1.5 \times 10^{-6}\ M_\odot\ \mathrm{yr}^{-1}$ and that the maximum value of $\alpha \sim 0.3$ (Mastrodemos & Morris 1999), the expected $\dot{M}_j \lesssim 4.5 \times 10^{-8}\ M_\odot\ \mathrm{yr}^{-1}$.

Hence, our significantly higher (about a factor of 7) jet mass-loss rate indicates that the accretion is occurring from the central equatorial disklike structure in Hen 2-90, where the densities are likely to be significantly higher than in the AGB wind. Such dense equatorial structures characterized by mass-loss rates as high as $\sim 3 \times 10^{-5}\ M_\odot\ \mathrm{yr}^{-1}$ have been found in several PPNs (Meixner et al. 1997). The expansion velocity of the equatorial structure in Hen 2-90 may also be smaller than that of the AGB wind, further enhancing the accretion rate. The observed minimum age of the jet (1400 yr; S02) sets a lower limit on the age of the central equatorial disklike structure, which must be taken into account by any formation scenario for the latter.

6. SUMMARY AND CONCLUSIONS

We have presented numerical simulations of a cylindrical jet interacting with a spherical AGB wind in order to produce the bipolar, knotty jet seen in Hen 2-90. In our models, the jet has a radius of 125 AU and an average velocity of 300 km s^{-1}, while the AGB wind has an expanding velocity of 10 km s^{-1} and a mass-loss rate of $1.5 \times 10^{-6}\ M_\odot\ \mathrm{yr}^{-1}$. Periodic variations in the jet density and/or velocity with a period of 43 yr produce a chain of knotty structures along the jet axis.

Comparing the Hα emission derived from our models to that in the observations of Hen 2-90 in detail, we find the following:

1. Nonmagnetized jets with density (model 1) or velocity (model 2) variations do not adequately reproduce the observed structure of the Hen 2-90 jet. In model 1, with a jet average mass-loss rate of $2.1 \times 10^{-7}\ M_\odot\ \mathrm{yr}^{-1}$, and initial length and mass of Gaussian pulse of 271 AU and $2.7 \times 10^{-6}\ M_\odot$, respectively, the H$\alpha$ emission in the knots peaks at the tail but not at the center of the knots, inconsistent with the observations, and the knot intensity decreases with distance from center faster than the observations. In model 2, with a jet average mass-loss rate of $2.7 \times 10^{-7}\ M_\odot\ \mathrm{yr}^{-1}$ and a sinusoidal velocity variation of ± 15 km s^{-1}, the variation of knot intensity with distance from center is in better (but still not adequate) agreement with the observations. However, the knots are now shorter in the longitudinal direction and wider in the transverse direction than the observations.
2. A nonmagnetized jet with variations in both density and velocity (model 3) produces knots whose length and width are in better agreement with the observations than models 1 and 2; however, the emission in this model still peaks at the tail of the knots, inconsistent with the observations, and the Hα intensity still decreases with distance from center faster than observed.
3. A model (model 4) of a magnetized jet (having a toroidal field with a maximum value of $\sim$0.6 mG) with small periodic variations in velocity (as in model 2) produces the best match with the knotty structures seen in the Hen 2-90 jet. The magnetic pressure expands the knots along the jet axis, whereas the magnetic tension produces the required confinement of the transverse expansion of the knots, bringing their overall shapes in good agreement with the observations.
4. The average mass-loss rate in the jet has to have steadily decreased with time (i.e., was higher by roughly a factor of 3, 600 yr ago) in order to reproduce the observed decrease in jet emission with distance from the center (model 5).
5. The leading bow shock is not observed in the ground-based images most likely because it lies beyond the Strömgren radius along the jet axis.

We thank the anonymous referee for his insightful comments that helped us to improve this paper, and Noam Soker for his comments on an earlier version of this paper. We thank Martin A. Guerrero for conversations about line widths in Hen 2-90 from ground-based observations. This work was performed while C.-F. L. held a National Research Council Research Associateship Award at the Jet Propulsion Laboratory, Caltech. R. S. acknowledges support by NASA through a Long Term Space Astrophysics grant (no. 399-20-61-00-00) and STScI grant GO-09102.01-A.

REFERENCES

Begelman, M. C. 1998, ApJ, 493, 291
Blackman, E. G., Frank, A., & Welch, C. 2001, ApJ, 546, 288
Blanford, R. D., & Payne, D. G. 1982, MNRAS, 199, 883
Calvet, N., Hartmann, L., & Strom, S. E. 2000, in Protostars and Planets IV, ed. V. Mannings, A. P. Boss, & S. S. Russell (Tucson: Univ. Arizona), 377
Cerqueira, A. H., & de Gouveia dal Pino, E. M. 1999, ApJ, 510, 828
Frank, A., Lery, T., Gardiner, T. A., Jones, T. W., & Ryu, D. 2000, ApJ, 540, 342
Frank, A., Ryu, D., Jones, T. W., & Noriega-Crespo, A. 1998, ApJ, 494, L79
García-Segura, G., López, J. A., & Franco, J. 2001, ApJ, 560, 928

García-Segura, G., López, J. A., & Franco, J. 2003, Rev. Mexicana Astron. Astrofis. Conf. Ser., 15, 12
Guerrero, M. A., Miranda, L. F., Chu, Y., Rodríguez, M., & Williams, R. M. 2001, ApJ, 563, 883 (G01)
Hartigan, P., Morse, J. A., & Raymond, J. 1994, ApJ, 436, 125
Hartmann, L., Calvet, N., Gullbring, E., & D'Alessio, P. 1998, ApJ, 495, 385
Kaler, J. B., & Jacoby, G. H. 1991, ApJ, 372, 215
Konigl, A., & Pudritz, R. E. 2000, in Protostars and Planets IV, ed. V. Mannings, A. P. Boss, & S. S. Russell (Tucson: Univ. Arizona), 759
Lind, K. R., Payne, D. G., Meier, D. L., & Blandford, R. D. 1989, ApJ, 344, 89
Mastrodemos, N., & Morris, M. 1999, ApJ, 523, 357
Meixner, M., Skinner, C. J., Graham, J. R., Keto, E., Jernigan, J. G., & Arens, J. F. 1997, ApJ, 482, 897
Mellema, G., & Frank, A. 1995, MNRAS, 273, 401
Morris, M. 1987, PASP, 99, 1115
Preite-Martínez, A., Acker, A., Koeppen, J., & Stenholm, B. 1991, A&AS, 88, 121
Raga, A. C., Binette, L., Canto, J., & Calvet, N. 1990, ApJ, 364, 601
Raga, A. C., Velázquez, P. F., Cantó, J., & Masciadri, E. 2002a, A&A, 395, 647
Reipurth, B., Bally, J., & Devine, D. 1997, AJ, 114, 2708
Reipurth, B., Heathcote, S., Morse, J., Hartigan, P., & Bally, J. 2002, AJ, 123, 362
Sahai, R., Brillant, S., Livio, M., Grebel, E. K., Brandner, W., Tingay, S., & Nyman, L.-Å. 2002, ApJ, 573, L123 (S02)
Sahai, R., & Nyman, L. 2000, ApJ, 538, L145
Sahai, R., & Trauger, J. T. 1998, AJ, 116, 1357
Shu, F. H., Najita, J. R., Shang, H., & Li, Z.-Y. 2000, in Protostars and Planets IV, ed. V. Mannings, A. P. Boss, & S. S. Russell (Tucson: Univ. Arizona), 789
Sod, G. A. 1978, J. Comput. Phys., 27, 1
Stone, J. M., & Hardee, P. E. 2000, ApJ, 540, 192
Stone, J. M., & Norman, M. L. 1992, ApJS, 80, 791